ACS NANO

www.acsnano.org

ARTICLE

Rapid Cellular-Resolution Skin Imaging with Optical Coherence Tomography Using All-Glass Multifocal Metasurfaces

Jingjing Zhao, Aidan Van Vleck, Yonatan Winetraub, Lin Du, Yong Han, Sumaira Aasi, Kavita Yang Sarin, and Adam de la Zerda*

Cite This: *ACS Nano* 2023, 17, 3442−3451

Read Online

ACCESS | Metrics & More | Article Recommendations | Supporting Information

ABSTRACT: **Cellular-resolution optical coherence tomography (OCT) is a powerful tool offering noninvasive histology-like imaging. However, like other optical microscopy tools, a high numerical aperture (N.A.) lens is required to generate a tight focus, generating a narrow depth of field, which necessitates dynamic focusing and limiting the imaging speed. To overcome this limitation, we developed a metasurface platform that generates multiple axial foci, which multiplies the volumetric OCT imaging speed by offering several focal planes. This platform offers accurate and flexible control over the number, positions, and intensities of axial foci generated. All-glass metasurface optical elements 8 mm in diameter are fabricated from fused-silica wafers and implemented into our scanning OCT system. With a constant lateral resolution of 1.1 μm over all depths, the multifocal OCT triples the volumetric acquisition speed for dermatological imaging, while still clearly revealing features of stratum corneum, epidermal cells, and dermal-epidermal junctions and offering morphological information as diagnostic criteria for basal cell carcinoma. The imaging speed can be further improved in a sparse sample, e.g., 7-fold with a seven-foci beam. In summary, this work demonstrates the concept of metasurface-based multifocal OCT for rapid virtual biopsy, further providing insights for developing rapid volumetric imaging systems with high resolution and compact volume.**

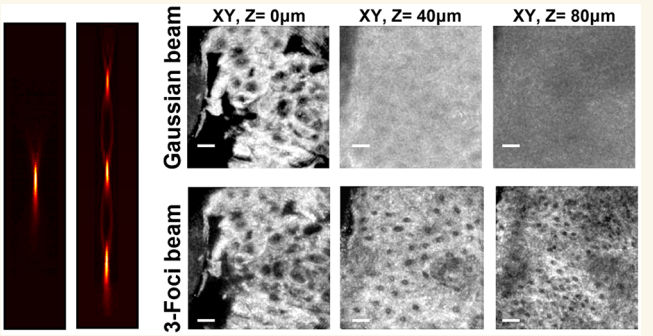

KEYWORDS: *all-glass metasurface, multifocal beam, phase change materials, optical coherence tomography, virtual biopsy, cellular resolution, noninvasive imaging*

In the past three decades, optical coherence tomography (OCT) has evolved into a versatile platform for noninvasive imaging, impacting a variety of biomedical fields, including ophthalmology,[1] cardiology,[2] angiography,[3] neuroscience,[4] gastroenterology,[5] dentistry,[6] and dermatology.[7] Although OCT has a millimeter-scale depth detection range, it suffers from a limited depth of focus (DOF) especially when a high numerical aperture (N.A.) lens is used to achieve cellular resolution. This weakness makes dynamic focusing[8,9] crucial for high-resolution 3D imaging, where the focus is axially translated through the scattering tissue and the volumetric image is reconstructed after through Z-stacking. However, dynamic focusing does not utilize the full depth of OCT's detection range and lowers its 3D imaging rate. Current approaches to solve this limitation center around methods for extending the DOF, including digital focusing,[10,11] Bessel beams,[12,13] annular phase filters,[14,15] and the multibeam method.[16] Generally, these approaches suffer from a myriad of issues including a loss in signal-to-noise ratio (SNR), low photon efficiency, performance degradation in dense samples (e.g., skin), and artifacts caused by sidelobes or axial-intensity oscillation. Previously, we developed a needle-shaped beam (NB) with a 20× objective to extend the DOF in OCT[17,18] for dermatological imaging. However, the resolution of a 20× lens is insufficient for disease diagnosis in some human skin disorders, necessitating a beam focused via a 40× objective. However, 40× objective NBs have significantly reduced energy efficiency, which result in a low SNR.

Received: September 25, 2022
Accepted: February 3, 2023
Published: February 6, 2023

https://doi.org/10.1021/acsnano.2c09542
ACS Nano 2023, 17, 3442−3451

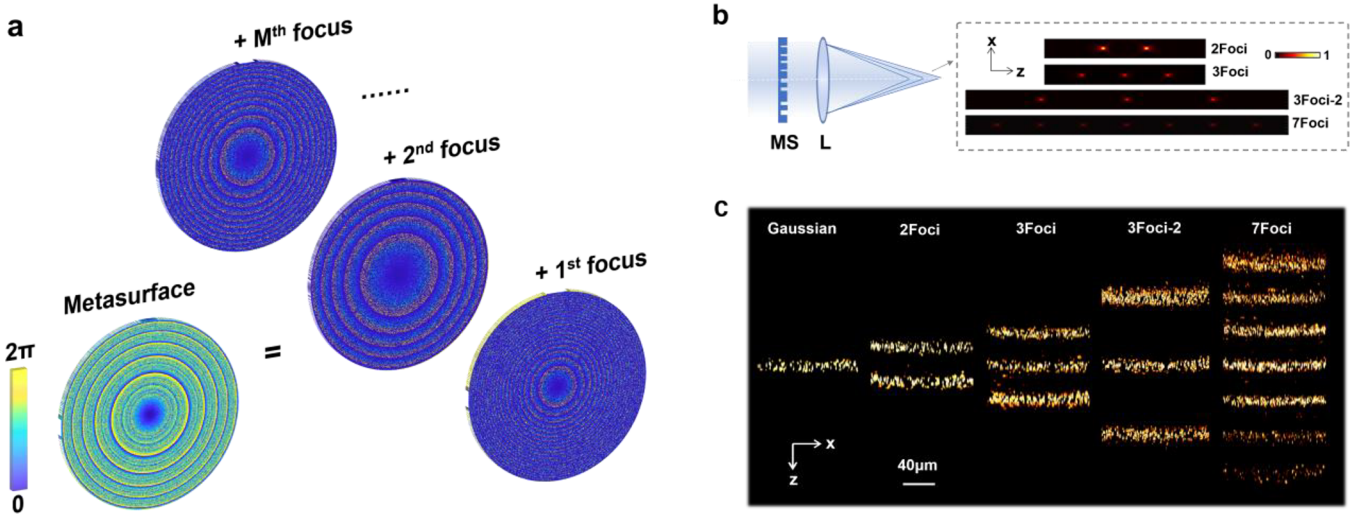

Figure 1. Principle of multifocal metasurface. (a) Multifocal metasurface composed of multiple phases of M foci via random spatial multiplexing. (b) Multifocal metasurfaces (MS) combine with a lens (L) to create hybrid lenses capable of generating multifocal beams. Simulations of four distinct multifocal beams are shown in linear scale. (c) With multifocal metasurfaces, OCT can generate two, three, or seven focal planes, as experimentally confirmed by OCT B-scans of 0.8 μm PS beads (displayed in logarithmic scale). Gaussian beam has one focal plane. The four multifocal beams correspond to the ones in (b).

To balance the trade-off between volumetric imaging speed and image quality, we propose a multifocal metasurface platform based on random spatial multiplexing, which can flexibly adjust the number, positions, and intensities of axial foci. This approach accelerates the imaging rate by generating several focal planes with minorly reduced image quality. We experimentally demonstrated metasurface-based multifocal OCT for rapid high-resolution skin imaging, which offers cellular resolution in the volumetric image while simultaneously granting a 3-fold increase in imaging rate compared to normal dynamic focusing. This tool can enable the diagnosis of more subtle skin conditions such as cutaneous autoimmune diseases, eczematous conditions, or melanocytic neoplasms which require higher magnification with cellular resolution for diagnosis.[19] More generally, this multifocal metasurface platform demonstrates promising applications across a broad range of microscopic systems, including confocal,[20] multiphoton,[21] and photoacoustic imaging,[22] where it is able to significantly increase the volumetric imaging speed while maintaining identical 3D spatial resolution.

Here, we utilize a metasurface rather than a diffractive optical element (DOE)[17] for two reasons. First, it has several fabrication advantages: its binary structure eliminates the mask alignment issue, the single lithography utilized is more efficient compared to the fabrication of the multilevel DOE,[23] and scalable fabrication is possible when using optical stepper lithography.[24] Second, the high pixel density of metasurface is more suitable for random spatial multiplexing, contributing to multifunctionality.[25] Metasurface features the manipulation of various light properties with ultrathin flat optical components[26] and shows potential in nearly every aspect of light research.[27,28] Applying flat optics of metasurface to biomedical imaging is an emerging trend[29] and has been studied in brightfield and differentiated microscopic imaging,[30] endoscopic OCT,[31] super resolution imaging,[32] two-photon imaging,[33] and extended-DOF OCT.[34] However, to the best of our knowledge, no previous work has demonstrated cellular-resolution imaging of human tissues using metasurfaces, and the value of metasurface in clinical diagnosis remains somewhat unclear. Furthermore, the current apertures of metasurface optics in biomedical imaging are relatively small (usually a few hundreds of micrometers in diameter), resulting in short focal lengths (or working distances), small fields-of-view (FOV), incompatibilities with scanners (e.g., galvo mirror), and an inability to deal with large diameter laser beams (e.g., millimeters in diameter). This work aims to solve these problems. We fabricated all-glass metasurface optics 8 mm in diameter from fused-silica wafer and integrated these flat optics into our scanning OCT system. We chose an all-silica design to simplify the fabrication process and selected fused silica due to its excellent transmission across the ultraviolet to infrared spectrum, including the OCT spectrum. Since a metalens has rampant chromatic dispersion,[35,36] especially in cases with a large diameter[37] and millimeter-level focal length,[38] we bypass a multifocal metalens in this work and instead use a hybrid lens[39,40] composed of a metasurface multifocal generator and an achromatic objective. We have experimentally proven the hybrid design is a pragmatic and reliable solution.

RESULTS AND DISCUSSION

Principle of Multifocal Beam. To axially generate multiple foci, as illustrated in Figure 1a, the metasurface phase is formulated as

$$P_{Meta}(x, y) = \sum_{m=1}^{M} \{[P_{Lens}(x, y, f_m) - P_{Lens}(x, y, f_o)] \times A_m(x, y)\}$$

where (x,y) is the planar coordinate, M is the foci number, f_m is the destinated focal position, f_o is the focal length of the objective cooperating with the multifocal metasurface, $P_{Lens} = 2\pi n[\sqrt{f^2 - (x^2 + y^2)} - f]/\lambda$ is the lens phase profile, λ is the light wavelength, n is the diffractive index of the surroundings, and $A_m(x,y)$ is a binary matrix working as the allocator to randomly assign metasurface pixels to different foci. The combination of multifocal metasurface and the objective in Figure 1b gives the phase modulation of $\sum_{m=1}^{M}[P_{Lens}(x, y, f_m) \times A_m(x, y)]$. Assuming an incident

https://doi.org/10.1021/acsnano.2c09542
ACS Nano 2023, 17, 3442−3451

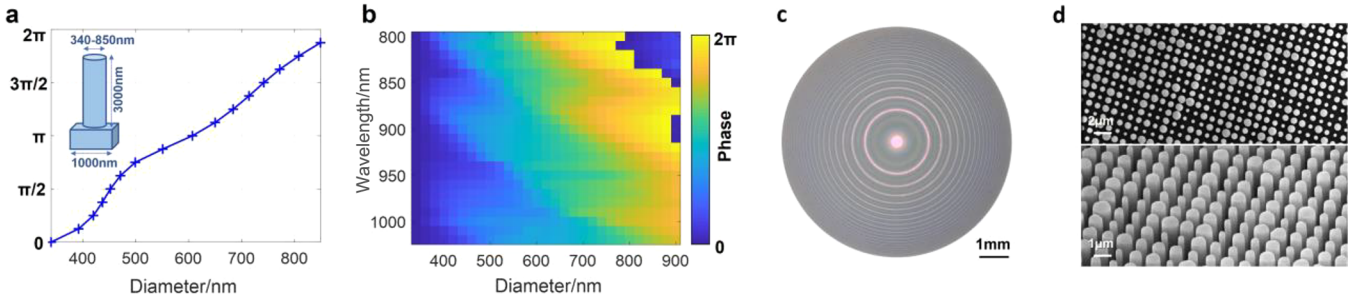

Figure 2. Metasurface design and fabrication. (a) Phase modulation library of SiO_2 nanopillars with varying diameters ranging from 340 to 850 nm on the silica substrate. (b) Simulated phase map of the various nanopillar diameters for the wavelengths 800−1050 nm. (c) An optical photograph of the fabricated metasurface. (d) SEM images of the nanopillars.

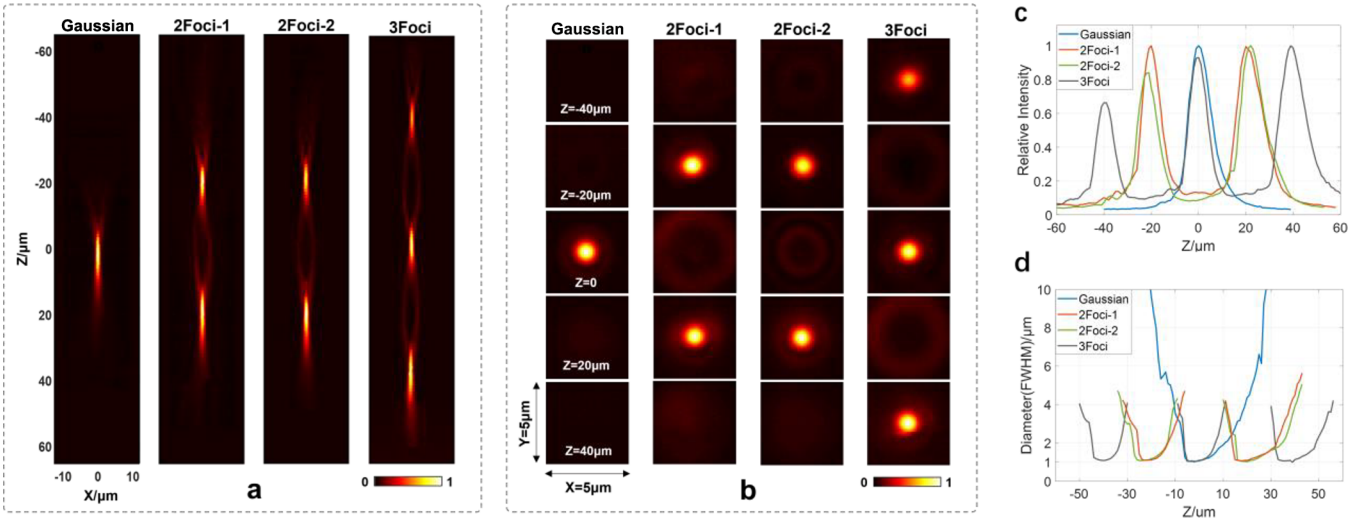

Figure 3. Characterization of multifocal beams. Beam profiles of Gaussian beam, two-foci beam 1 (2Foci-1), two-foci beam 2 (2Foci-2) and three foci beam (3Foci) in (a) *XZ* plane and (b) *XY* planes and their (c) axial intensity profiles and (d) beam diameters along the depth.

beam has a Gaussian amplitude of $G(x,y)$, the beam modulated by the metasurface phase is

$$\sum_{m=1}^{M} \{G(x,y) \times \exp[i \times P_{Lens}(x,y,f_m) \times A_m(x,y)]\}$$
$$= \sum_{m=1}^{M} \{G(x,y) \times \exp[i \times P_{Lens}(x,y,f_m)] \times A_m(x,y)\}$$

We set $\{G(x,y) \times \exp[i \times P_{Lens}(x,y,f_m)]\}$ as $F_{Lens}(x,y,f_m)$. The generated light field is $\sum_{m=1}^{M} \{FT[F_{Lens}(x,y,f_m)] \otimes FT[A_m(x,y)]\}$ and FT denotes Fourier transform. $FT[F_{Lens}(x,y,f_m)]$ is the function for the focus located at f_m. Here we use $F(x,y,f_m)$ to represent $FT[F_{Lens}(x,y,f_m)]$ for simplification. Since the distribution of $A_m(x,y) = 1$ is random over the entire metasurface, $FT[A_m(x,y)]$ approximates $\delta(x,y) \times R_m$, where $\delta(x,y)$ is the unit impulse function and R_m is the ratio between the number of pixels allocated to focus f_m and the total number of the metasurface pixels. The light field is expressed as $\sum_{m=1}^{M} [F(x,y,f_m) \times R_m]$, implying multiple foci are generated from f_1, ...f_M, and the energy distribution among the foci is controlled by R_1, ...,R_M. As demonstrated by the simulated multifocal beams in Figure 1b, the number and locations of foci can be flexibly changed. In Figure 1b, incident light energy is equally allocated among foci, and focal intensity is inversely proportional to the square of the number of foci. We fabricated four multifocal metasurfaces which correspond with the four multifocal beams in Figure 1b and tested them in our OCT system (Figure S1a). With the help of the multifocal metasurfaces, the OCT can generate two, three, or even seven focal planes, as experimentally demonstrated by OCT B-scans (XZ planes) of 0.8 μm polystyrene (PS) beads in Figure 1c.

Metasurface Implementation. The schematic of metasurface design process is given in Figure S2a. We created metasurfaces from a thin fused silica plate with SiO_2 cylindrical nanopillars of various diameters to modulate phase delay. Rotationally symmetric elements ensure nonpolarization sensitivity. The relative phase delay of transmitted light in nanopillars with varying diameters was calculated with respect to light propagation in the narrowest nanopillar. These calculations were performed by simulations using the finite element analysis tool (electromagnetic waves frequency domain, COMSOL Multiphysics). Our OCT system has a light source centered at 910 nm with a bandwidth of 200 nm and a 40× water-immersion objective (UMPLFLN40XW, Olympus) of a focal length of 4.5 mm. We first built the transmission phase library for 910 nm light in Figure 2a, and pixel size is 1 μm and each pixel has a nanopillar with a constant height of 3.0 μm. The phase delay at 910 nm is modulated from 0 to 2π by changing the nanopillar diameter

https://doi.org/10.1021/acsnano.2c09542
ACS Nano 2023, 17, 3442−3451

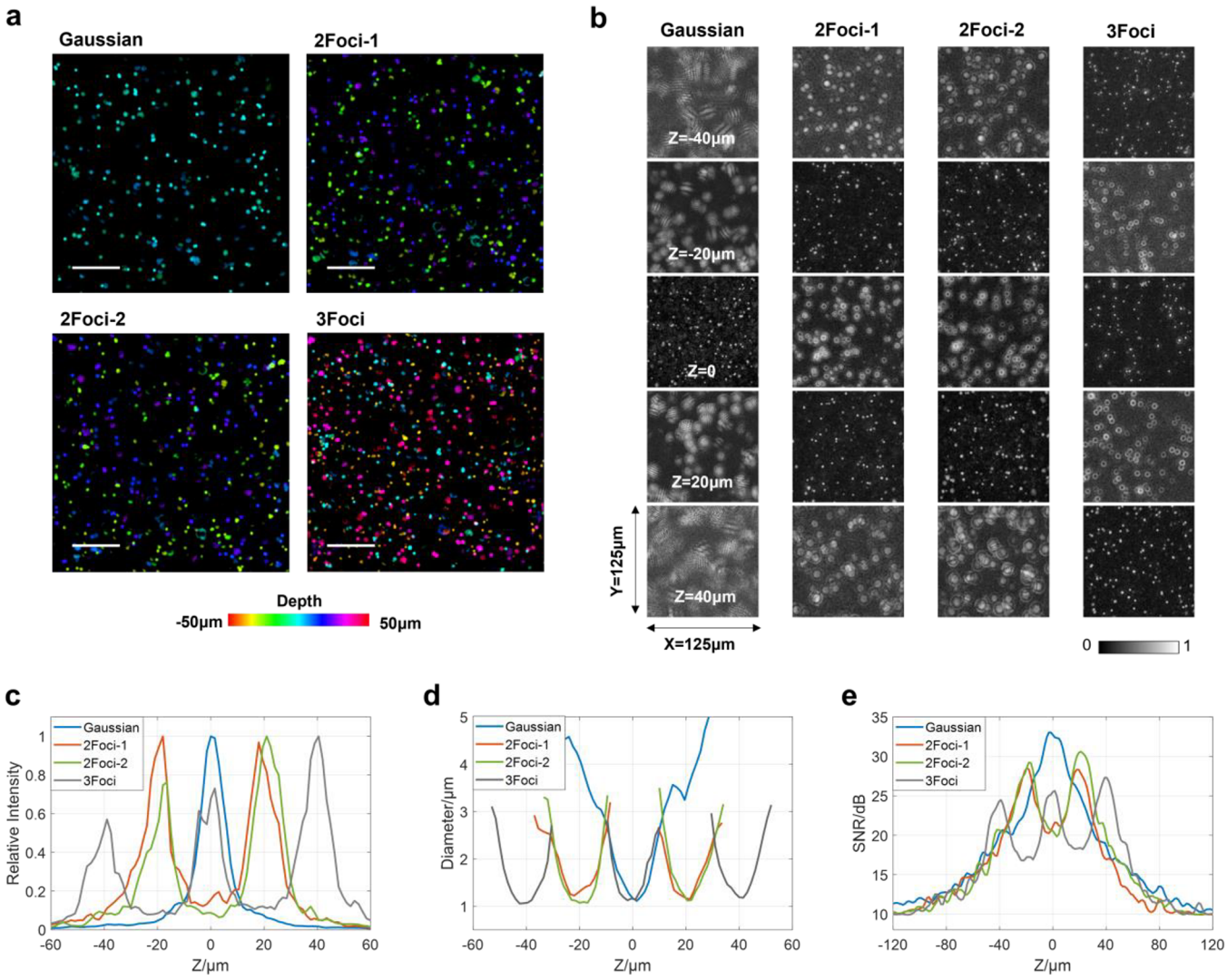

Figure 4. Volumetric imaging of 0.8 μm PS beads by Gaussian, two-foci (2Foci-1 and 2Foci-2), and three-foci (3Foci) beams. (a) Maximum intensity projections, scale bar = 25 μm. (b) *XY* images at different depths by Gaussian, 2Foci-1, 2Foci-2, and 3Foci beams. (c) The axial intensity profiles, (d) bead diameters at different depths, and (e) the SNR ratios along the depth are measured from the volumetric images.

from 340 to 850 nm. We chose 16 discrete diameters to cover $[0, 2\pi]$, achieving the phase step of $\pi/8$, and then scanned the entire wavelength range generating a phase map shown in Figure 2b. Chromatic aberration is discussed in Figure S3. The fabrication was based on e-beam lithography and inductively coupled plasma (ICP) etching (Figure S2b). The fabricated pillars have a taper angle around 2° (Figure S2c). The disparity between the ideal vertical sidewall and the real tapered sidewall was accounted for in the aforementioned simulations. Figure 2c gives a full view of the metasurface plate (VHX-6000, Keyence) and Figure 2d is a scanning electron micrograph (Nova NanoSEM 450, FEI) revealing the nanopillars.

Multifocal Beams for OCT. Our multifocal metasurface shows significant design flexibility. The number, axial locations, and energy allocation of independent foci are readily controlled by the parameters of f_1, ...f_M and R_1, ...,R_M. Since the samples for OCT skin imaging are usually dense with strong light absorption, we purposely limit the number of foci to achieve a higher power of each focus. As shown in Figure 3, we chose three multifocal beams for OCT imaging: the two foci beam 1 (2Foci-1) has an axial interval of 40 μm with metasurface pixels equally allocated to both foci (R_1 = 50%, R_2 = 50%), the two foci beam 2 (2Foci-2) has an identical interval of 40 μm and different pixel ratios (R_1 = 45%, R_2 = 55%), and the three foci beam (3Foci) similarly has a 40 μm interval with ratios R_1 = 27%, R_2 = 33%, and R_3 = 40%. The profiles of the three beams were measured using the tool shown in Figure S1b with the OCT light source (910 ± 100 nm). As proven by the *XZ* profiles in Figure 3a, the foci positions of all three multifocal beams are coincident with their design. Figure 3b shows the beam's cross-sectional profiles at five depths, demonstrating each focus has a circular Gaussian profile. The axial intensity distributions of the normal Gaussian beam and the three multifocal beams are given in Figure 3c. The intensity ratio between the two foci of 2Foci-1 is 50:50, the intensity ratio of 2Foci-2 is 46:54, and the intensity ratio of 3Foci is 25:36:39. The experimental ratios were concordant with the designed values, demonstrating the accuracy of our method. Figure 3d compares the beam diameters of the multifocal beams and the focused Gaussian beam. All foci have a diameter of 1.0−1.1 μm and a DOF of 6 μm. In Figure 3 and following Figure 4, the focal position of the 40× objective is set as Z = 0. The focal lengths for 2Foci beams and 3Foci beams are respectively 4.5 mm ±20 μm as well as 4.5 mm + (−40 μm, 0

https://doi.org/10.1021/acsnano.2c09542
ACS Nano 2023, 17, 3442−3451

μm, 40 μm). All the foci have an identical focal size because of negligible differences in focal lengths.

The Gaussian beam and the three multifocal beams were characterized in our OCT system (Figure S1a) using 0.8 μm PS beads. The resultant B-scans are shown in Figure 1c. The maximum intensity projections of the beads along the depth direction (Figure 4a) shows that the Gaussian beam can only acquire clear bead profiles from a thin depth layer with a relatively low number of beads in the field-of-view (FOV). Contrastingly, the 2Foci-1 and 2Foci-2 beams can clearly resolve beads from two focal planes, providing significantly more useful information in the same data acquisition process. Similarly, the 3Foci beam can reveal the most beads, as it captures data along three focal planes. Figure 4b gives the *XY*-planes at five depths. While the Gaussian beam distinguishes beads clearly at $Z = 0$, the bead profiles enlarge significantly in the unfocused depths. Both two-foci beam profiles resolve the beads accurately at $Z = -20$ and 20 μm, and three-foci beam shows clear resolution at $Z = -40$ μm, 0, and 40 μm. Additional bead phantom imaging details are available in Figures S4−S7. Axial intensities of the four beams were measured from the bead phantom volume and are plotted in Figure 4c. As previously stated, the multifocal beam is formulated as $\sum_{m=1}^{M}[F(x, y, f_m) \times R_m]$ and the intensity is predicted by $\left\{\sum_{m=1}^{M}[F(x, y, f_m) \times R_m]\right\}^2$. The intensity ratio between the two foci of 2Foci-1 is 51:49, close to the design of $(50{:}50)^2$ = 50:50. The intensity ratio in 2Foci-2 is 41:59 similar to the designed $(45{:}55)^2$ = 40:60. The ratio in 3Foci is 25:31:44 and is approximate to the design of $(27{:}33{:}40)^2$ = 21:31:48. It is worth mentioning that the intensity ratio in the camera-acquired images (Figure 2) is linear to R_1, ...,R_M, since the light source is wideband low-coherence and the camera imaging has no dispersion compensation (digitally or physically) that is commonly used in OCT. Bead diameters were measured to evaluate resolution (Figure 4d). All beams present comparable resolution power around their focal planes with the measured bead diameter around 1.1−1.2 μm. The signal-to-noise ratios (SNRs) along the depths of 3D bead images are shown in Figure 4e. Here, SNR = (peak intensity − average background intensity) ÷ standard deviation of background intensity. The multifocal beams outperform Gaussian beam in SNR at their focal planes.

For OCT virtual biopsy, 2Foci-2 and 3Foci beams were selected for two reasons. First, the intensity of a single focus is proportional to $(R_m)^2$. In other words, basically focal intensity is inversely proportional to the square of number of foci. Ideally, the signal intensity of a two-foci beam is around 25% of that in a Gaussian beam, while a three-foci beam is roughly 10% of a Gaussian's intensity. Also, the maximum SNR of a multifocal beam decreases with increasing foci number, as proved in Figure 4e. We tested two-, three-, four-, five-, and seven-foci beams and found two-foci and three-foci beams are the most pragmatic and reliable for dense and highly scattering samples. Additionally, the efficiency of a metasurface is not 100%, and thus it is critical to accurately determine the number to ensure sufficient energy for each focus. According to our OCT experiments, the efficiency of two-foci metasurface is about 70% and the efficiency of three-foci metasurface plate is about 85%. Second, 2Foci-2 and 3Foci beams are designed to deliver more energy to deeper focus/foci, allowing us to enhance SNR from deep regions in highly light-absorbing samples.

Rapid High-Resolution Cellular Imaging. Currently, cellular-resolution imaging is achieved with a high N.A. lens and is limited within the lens' short DOF. OCT imaging using a 40X objective was conducted on normal skin obtained from the nasal side-wall of a 74-year-old man (Figure 5a). The focal plane was located at the skin surface ($Z = 0$). While the features of the stratum corneum are clearly visualized, the images from the epidermis area are too blurry to distinguish, as illustrated by the *XY* planes at $Z = 40$ and 80 μm. With the two-foci beam (2Foci-2), two focal planes are generated in the B-scan (Figure 5b), and stratum corneum at $Z = 0$ and the epidermal cells at $Z = 40$ μm are exactly profiled. The OCT system utilizing the three-foci beam (3Foci) can reliably acquire cellular-resolution images from three focal planes simultaneously. Cells are easily resolved at the discrete depths of $Z = 0$, $Z = 40$ μm, and $Z = 80$ μm. These experimental results demonstrate that multifocal beams can collect highly detailed image data from multiple planes, gathering 2- to 3-fold the volume of a Gaussian beam under identical parameters.

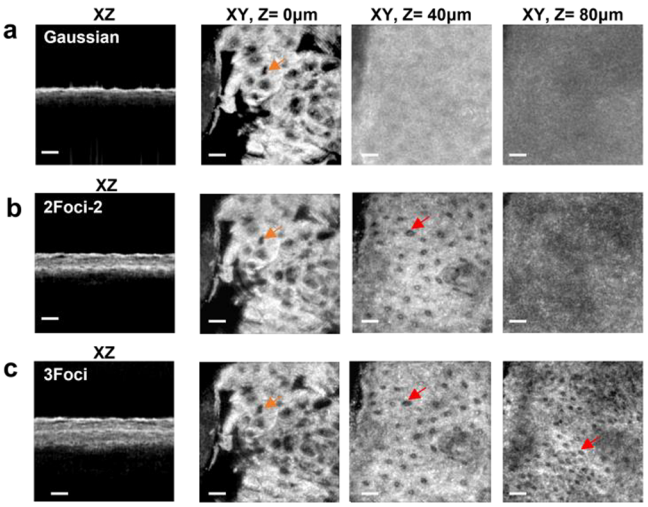

Figure 5. OCT imaging of normal human nasal skin by (a) Gaussian, (b) two-foci (2Foci-2), and (c) three-foci (3Foci) beams. The Gaussian beam is focused on the skin's surface ($Z = 0$) and one bright layer is observed in B-scan (*XZ*-plane). The first focus of 2Foci-2 and 3Foci beams are placed on the skin's surface with two and three focal planes captured in B-scans. At $Z = 0$, all three beams resolve identical structures in the stratum corneum, e.g., the feature marked by the orange arrows. Both 2Foci-2 and 3Foci reveal epidermal cells at $Z = 40$ μm. 3Foci beam further resolves cells at $Z = 80$ μm. Several epidermal cells are indicated by red arrows. Scale bar = 30 μm.

To perform high-resolution volumetric imaging, dynamic focusing is utilized. The focal plane is axially translated to scan consecutive stepwise depths. After every translation, the sample is imaged volumetrically again and only the layers within the DOF are extracted to store. Finally, all the stored layers are digitally reconstructed to form the entire high-resolution 3D image. In theory, the number of axial movements (Z-stacks) is inversely proportional to the number of foci of the beam. Theoretically, the two-foci or three foci metasurface beams only requires half or one-third of the number of Z-stacks compared to the Gaussian beam, allowing significantly faster cellular-resolution skin imaging.

https://doi.org/10.1021/acsnano.2c09542
ACS Nano 2023, 17, 3442−3451

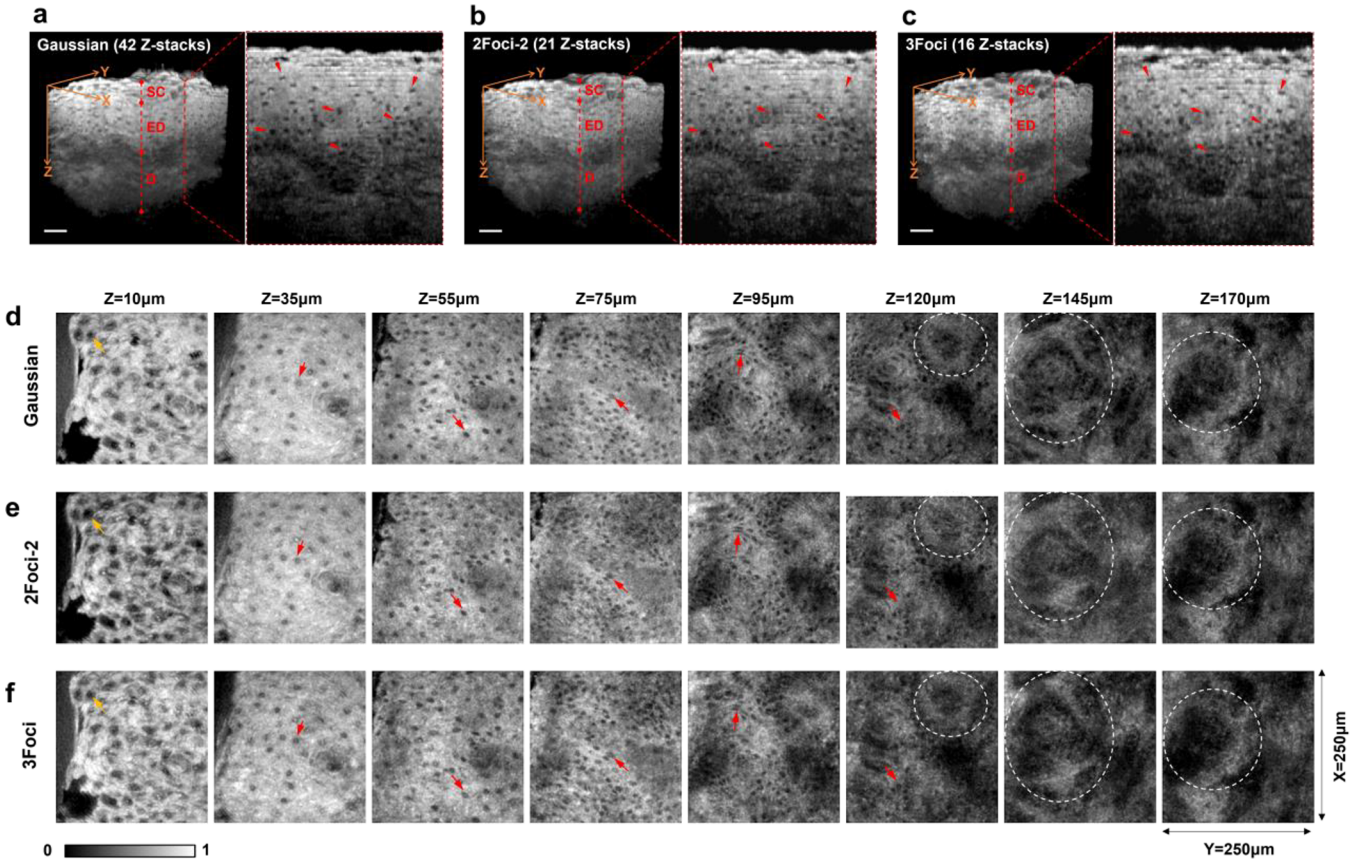

Figure 6. Volumetric imaging of normal human nasal skin by Gaussian with 42 Z-stacks, two-foci (2Foci-2) with 21 Z-stacks, and three-foci (3Foci) beams with 16 Z-stacks. The sample volume is 250 μm × 250 μm × 250 μm ($X \times Y \times Z$). (a–c) In the 3D images captured by the three beams, the stratum corneum, epidermis, and dermis are equally and clearly identified. The extracted B-scan (located at Y = 125 μm) shows the same cells can be identified across all three volumes, with some examples denoted by red arrows. Scale bar = 40 μm. (d–f) *XY* images at different depths across all three beams demonstrate equivalent image qualities, showing the features in the stratum corneum (marked by orange arrows), epidermal cells (red arrows), and dermal-epidermal junctions (white circles). SC, stratum corneum; ED, epidermis; D, dermis.

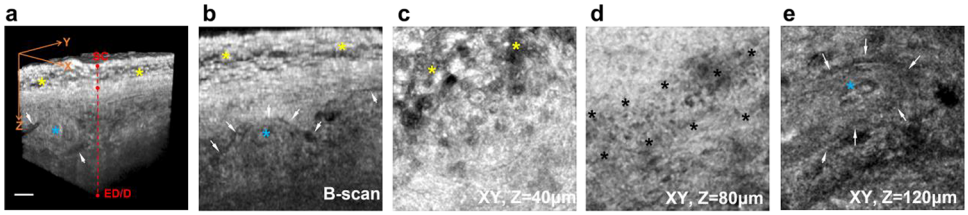

Figure 7. Volumetric imaging of a BCC nasal sample by the three-foci (3Foci) beam (imaging volume, $X \times Y \times Z$ = 250 μm × 250 μm × 250 μm). (a) 3D imaging, scale bar = 40 μm. (b) The B-scan (*XZ* plane) located at Y = 120 μm. (c–e) The *XY* cross sections at three depths. SC, stratum corneum; ED, epidermis; D, dermis.

The Z-stacked volumetric images of the normal human skin sample are shown in Figure 6. The sample volume is 250 μm × 250 μm × 250 μm ($X \times Y \times Z$) and the axial interval of dynamic focusing is 6 μm. The Gaussian beam was initially focused at the skin's surface (Z = 0) and was axially translated to Z = 250 μm in 6 μm steps between scans, generating 42 Z-stacks. For the two-foci beam (2Foci-2), its two foci were initially located on Z = 0 and Z = 40 μm respectively, and it scanned the depth range 0–80 μm with the same step interval of 6 μm. In order to avoid scanning previously scanned regions, its foci were relocated to Z = 80 μm and Z = 120 μm respectively, whereafter it scanned the depth range of 80–160 μm. This jumping pattern was then employed across the entire depth range of 250 μm, generating 21 Z-stacks. Similarly, the three-foci beam (3Foci) first scanned the depths from Z = 0 to Z = 120 μm, and then used its second and third foci to detect the remaining area (from Z = 120 μm to Z = 250 μm). The first focus was not applied to the deeper area in this sample as the first focus's SNR was relatively weak. The 3Foci beam captured 16 Z-stacks. Referring to Figure 6a–c, all three beams can generate high-quality cellular-resolution 3D images where the stratum corneum, epidermis, and dermis are easily recognizable. We can identify the exact same cells across all three volumes (marked by red arrows) in extracted B-scans. In Figure 6c, some deep cells seem a little larger since 3Foci beam's SNR is lower, as shown in Figure 4e, thus weak signals from a deep cell (especially for its core area) become low observable or may be lost in the B-scan image. Figure 6d–f

https://doi.org/10.1021/acsnano.2c09542
ACS Nano 2023, 17, 3442–3451

presents the *XY* images at different depths in the volumetric reconstructed scans captured by Gaussian, 2Foci-2, and 3Foci beams. At $Z = 10$ μm, identical landmarks in the stratum corneum are identified by the three beams; one example is denoted by orange arrows. In the epidermal layer (from $Z = 35$ μm to $Z = 95$ μm), numerous individual cells are revealed and identical cells (such as the ones pointed by red arrows) exist among the images taken by all three beams. In the dermis layer (from $Z = 195$ μm to $Z = 170$ μm), the structures of dermal-epidermal junction (marked by white circles) are captured. More detailed comparisons among the three beams are given in Figure S8 and Video S1. In summary, the above experimental analysis proves that the two-foci and three-foci beams can produce volumetric images highly comparable with the Gaussian beam, while only requiring half or one-third of the volumetric acquisition time that Gaussian beam needs.

Figure 7 shows OCT imaging of a basal cell carcinoma (BCC) sample obtained from the nose of a 75-year-old man. The image was captured via the three-foci (3Foci) beam. Compared to the normal skin sample shown before, the BCC sample demonstrates a thick stratum corneum and unclear boundary between tumor keratinocyte cells and surrounding stroma (Figure 7a). The stratum corneum displays an irregular honeycomb pattern (yellow asterisks in Figure 7a–c). In Figure 7a,b,e, single bright tumor islands (blue asterisks) surrounded by dark peritumoral clefts (white arrowheads) are found. Figure 7d shows distinct tumor keratinocytes crowded together with no intervening stromal cells (black asterisks). These findings are consistent with characteristics of BCC observed using the high-resolution reflectance confocal microscope (RCM) to observe skin cancers.[41−43] In RCM, the above abnormal morphological information can be diagnostic criteria for BCC. The same sample was also imaged using Gaussian beam and two-foci beam (2Foci-2) in Figure S9 and Video S2. The numbers of Z stacks for the three beams are 42, 21, and 14, respectively.

Discussion. We examined two additional properties of the multifocal metasurface developed in this work. The first is see how many foci at most can be generated using this method. In our experiments, the record is seven foci, as shown in Figure S10. We designed the device with equal energy distribution among the seven foci, but the real uniformity did not perfectly match the hypothesized profile (Figure S10a,b). Because the intensity of a single focus in the seven-foci beam is quite low (about 2% of the normal Gaussian beam in our experiments), the adverse influence of the fabrication errors becomes prominent. However, the diameters of foci still maintain close to Gaussian focal size (Figure S10c). While the OCT system is capable of producing seven focal planes in the bead phantom (Figure S10d–g), it is impractical for dense samples because of the weak focal intensity. The second exploration is to adjust this theoretical model for metalens. Referring to the above section of principle, we directly endowed the metasurface with the phase pattern $\sum_{m=1}^{M}[P_{Lens}(x, y, f_m) \times A_m(x, y)]$ in order to construct a multifocal metalens that does not require an independent objective. We fabricated a dual-focal metalens with focal lengths 4.4 mm and 4.6 mm (in water). The experimental results (Figure S11) show that it was capable of generating two foci with a narrow bandwidth light of 910 ± 10 nm but failed with a wider bandwidth 910 ± 100 nm. This is the result of serious chromatic dispersion, which can be corrected[44−46] at the cost of structural complexity and transmission efficiency. Our next work will focus on building an achromatic multifocal metalens. Due to their flat and thin construction, metalenses can effectively minimize the OCT probe, expanding the applications of OCT. Another approach to further improving OCT image quality is to apply adaptive optics[47] to multifocal beams by reducing the effect of incoming wavefront distortions due to tissues' inhomogeneity. Apart from OCT, the spatial-multiplexing method developed here for multifocal beams offers possibilities for multifunctional photonic devices or imaging.[48−50] By randomly allocating the pixels of a metaoptics for different groups, each group can not only be focused into a specific spatial area but also can be given with a different optical function or tailored for an independent imaging ability, such as polarization sensitivity, wavelength sensitivity, imaging a specific area, multichannel optical communication, or parallel optical computing.

CONCLUSIONS

In this work, we demonstrated the concept of metasurface-based multifocal OCT applied to rapid histology-like imaging (virtual biopsy). The multifocal OCT can triple the volumetric acquisition speed of high-quality cellular-resolution dermatologic imaging, with no degradation to spatial resolution. Sparce samples allow for even greater imaging speed increases, e.g., a 7-fold improvement with a seven-foci beam. The multifocal phase model we propose leverages random spatial multiplexing, which can flexibly and accurately manipulate the number, positions of foci, and intensities of independent foci. We developed a fabrication procedure for large (e.g., 8 mm in diameter) all-glass metasurface optics with fused silica wafer. In future work, we will develop achromatic multifocal metalenses to allow miniaturization of the OCT probe, and thus significantly more applications. The techniques developed in this work are not only practical for OCT applications but are also applicable to other microscopic systems, such as confocal, multiphoton, and photoacoustic imaging, where acceleration of the volumetric imaging speed would be beneficial. Briefly, this work provides prospects for developing rapid volumetric imaging systems with consistently high spatial resolution and compact volume.

METHODS

OCT System. As shown in Figure S1a, our OCT system is based on a commercial OCT instrument (Ganymede OCTP-900, Thorlabs) and the light source is centered at 910 nm with a bandwidth of 200 nm (EXR-9 continuum laser, NKT Photonics). The Gaussian beam diameter before entering the objective is 4.6 mm ($1/e^2$). Its acquisition rate is 30,000 A-scans/s. The imaging depth is 2 mm in air or 1.5 mm in water with 1024 pixels, thus the axial pixel size is about 2.0 μm in air and 1.5 μm in water, and the experimental axial resolution is 3 pixels (fwhm in linear scale). It is equipped with a 40× water immersion objective (UMPLFLN40XW, Olympus), offering a FOV of 0.5 mm × 0.5 mm with a good image quality. The laser power entering the objective aperture is controlled below 10 mW. For the experiments in Figures 4–6, pixel number in both the *X* and *Y* directions was chosen as 512, and FOV was set as 0.125 mm × 0.125 mm for bead imaging and 0.25 mm × 0.25 mm for skin imaging, respectively. During image reconstruction, a 2D Gaussian filter with a standard deviation of 2 pixels was applied for every *XY* image to reduce speckle noises. All OCT images were presented in log10 scale.

Metasuraface Fabrication. Figure S2a shows the fabrication procedure. Step 1: Use excimer laser (532 nm laser, 15W, 200 mm/s writing speed, 67 kHz with 80% duty factor, Delphi Laser) to divide one 4 in. fused silica wafter (4 in. in diameter, 500 μm thickness) into 12 1 in. circular plates, then clean by soaking the 1 in. plates in

https://doi.org/10.1021/acsnano.2c09542
ACS Nano 2023, 17, 3442−3451

piranha solution (9:1 H_2SO_4:H_2O_2) for 20 min at 120 °C. Step 2: Coat 400 nm PMMA-950-A4 photoresist onto the 1 in. plate with Headway spinner (1500 rpm, 1 min), and softback for 1.5 min at 180 °C. Step 3: Sputter 5 nm/10 nm gold (corresponding to e-beam current 5 nA/27 nA) onto the PMMA surface (Cressington sputter coater). Perform e-beam patterning with Raith Voyager (700 $\mu C/cm^2$ dose, e-beam current 5 nA/27 nA, e-beam step 10 nm/25 nm), which takes 2.5 h for a 5 mm-diameter pattern under the 5 nA current or 2.7 h for an 8 mm-diameter pattern under the 27 nA current. Remove gold deposition with gold etchant (Sigma-Aldrich) for 60 s, followed by two 60 s deionized (DI) water baths. Develop the exposed PMMA with MIBK/IPA 1:3 developer for 90 s, followed with 60 s IPA bath, 60 s DI water bath, and N_2 drying; postbake at 100 °C for 90 s. Step 4: Descum the developed silica plate with RIE (50 sccm Ar and 5 sccm O_2 at 50 W for 1 min, Oxford-RIE80). Deposit 200 nm chrome with e-beam evaporator (Kurt J. Lesker) at the rate of 0.3 nm/s. Step 5: Lift-off using two 5 min ultrasonic baths of PG remover, followed by one 60 s IPA bath and one 60 s DI water bath. Step 6: Etch the silica plate with the chrome mask using ICP (Plasma Therm Versaline: the parameters are 450 W ICP, 50 W BP, 38 sccm CHF_3, 16 sccm CF_4, 20 sccm Ar, 5 mT, 4T He, 10 °C electrode, 70 °C liner, 90 °C spool, 90 °C lip. The etching rate ≈2.8 nm/s, selectivity between silica and chrome ≈20). Step 7: Remove the remained chrome with chrome etchant (40 °C for 10 min) and clean the final silica metasurface plate with piranha solution for 10 min and successive DI water.

Beam Characterization. Beam profiles were measured by a microscope system shown in Figure S1b. Its magnification is 55.5 when using a 20× water immersion objective (UMPLFLN20XW, Olympus) with a 500 mm lens for imaging. The axial scanning step size was 1 μm for Gaussian, two-foci, and three-foci beams, 2 μm for the seven-foci beam, and 10 μm for the beams in Figure S9. The beam diameter (fwhm) in a 2D image is calculated as $2 \times \sqrt{A_{fwhm}/\pi}$, where A_{fwhm} is the area where the beam intensity is no less than the half of the maximum intensity (after background subtraction). The beam resolution in OCT system was tested with 0.8 μm PS beads. The resolution at specific depths was determined by the average diameter (fwhm in linear scale) of bead profiles. Each XY layer containing beads in a volumetric image was measured to determine the complete resolution profile of the target beam. Within each depth, about 100 beads were averaged to give reliable results.

Samples. The phantom used to characterize the multifocal beams in OCT was made by uniformly distributing 0.8 μm polystyrene (PS) beads (TP-08−10, Spherotech) in ultrasound gel (Aquasonic 100, Parker). The phantom was degassed with a centrifuge (15 min at 15,000 rpm, ST16-R, Thermo) with bead concentration around $1.5 \times 10^5/mm^3$. Human skin biopsies were obtained from discarded specimens from two patients undergoing Mohs Micrographic Surgery under IRB-48409. Two human skin samples were used in this paper, both of which were freshly procured from the Dermatologic Surgery Clinic at Stanford. Sample 1 was an adjacent normal skin sample from the right nasal dorsum of 74-year-old male patient and was collected from the nose as peripheral tissue dogears during surgery. Sample 2 was a basal cell carcinoma, collected from the nose of a consenting 75-year-old male patient. Both samples were prepared for imaging in an identical way. Following surgical excision, both were stored on ice in DMEM media and were immediately transported from the surgical clinic to the lab. Upon arrival at the lab, samples were removed from DMEM and placed face-down on a glass coverslip, so the epidermis lay flat on the surface of the glass. A 4% Agarose gel was then heated, and once liquid, poured into a histological cassette. The coverslip with the attached sample was then inverted above the cassette, submerging the sample in gel. Once the gel cooled and hardened, the coverslip was removed. This created a tissue bound within the gel, with the epidermal surface of the tissue upright and uncovered, ready for imaging.

ASSOCIATED CONTENT

Supporting Information

The Supporting Information is available free of charge at https://pubs.acs.org/doi/10.1021/acsnano.2c09542.

Metasurface-based OCT system setup; beam profiling system; metasurface fabrication schematic; chromatic aberration analysis; SEM of falling-down nanopillars of metasurface; volumetric imaging of microbeads by Gaussian beam, two-foci beams, and three-foci beam; *XY* images of human skin at different depths by Gaussian, two-foci, and three-foci beams; characteristics of the seven-foci beam; two-foci metalens characterization (PDF)

Video S1: Comparison of the volumetric imaging of human skin by Gaussian, two-foci, and three-foci beams (AVI)

Video S2: Comparison of the volumetric imaging of human skin by Gaussian, two-foci, and three-foci beams (AVI)

AUTHOR INFORMATION

Corresponding Author

Adam de la Zerda − *Department of Structural Biology, Stanford University School of Medicine, Stanford, California 94305, United States; Biophysics Program at Stanford, Molecular Imaging Program at Stanford, and The Bio-X Program, Stanford University, Stanford, California 94305, United States; The Chan Zuckerberg Biohub, San Francisco, California 94158, United States*; Email: adlz@stanford.edu

Authors

Jingjing Zhao − *Department of Structural Biology, Stanford University School of Medicine, Stanford, California 94305, United States*; orcid.org/0000-0003-0937-2751

Aidan Van Vleck − *Department of Structural Biology, Stanford University School of Medicine, Stanford, California 94305, United States*

Yonatan Winetraub − *Department of Structural Biology, Stanford University School of Medicine, Stanford, California 94305, United States; Biophysics Program at Stanford, Molecular Imaging Program at Stanford, and The Bio-X Program, Stanford University, Stanford, California 94305, United States*

Lin Du − *Department of Electrical Engineering and Computer Sciences, University of California, Berkeley 94720, United States*

Yong Han − *Department of Precision Instrument, Tsinghua University, Beijing 100084, China*

Sumaira Aasi − *Department of Dermatology, Stanford University School of Medicine, Stanford, California 94305, United States*

Kavita Yang Sarin − *Department of Dermatology, Stanford University School of Medicine, Stanford, California 94305, United States*

Complete contact information is available at: https://pubs.acs.org/10.1021/acsnano.2c09542

Author Contributions

J.Z. and A.d.l.Z. conceived the presented idea. J.Z. developed the theoretical analysis. J.Z., L.D., and Y.H. fabricated the metasurfaces. J.Z. and A.V.V. performed experiments. J.Z. processed the data. J.Z., A.V.V., S.Z.A, and K.Y.S. supervised

https://doi.org/10.1021/acsnano.2c09542
ACS Nano 2023, 17, 3442−3451

the human subjects protocol, prepared the specimens, and provided dermatologic input into interpretation of images. All the authors analyzed the experiments. J.Z., A.V.V., K.Y.S., and A.d.l.Z. cowrote the paper. All authors provided critical revision feedback to the manuscript.

Funding

United States Air Force (FA9550-15−1-0007), National Institutes of Health (NIH DP50D012179, K23CA211793), National Science Foundation (NSF 1438340), Damon Runyon Cancer Research Foundation (DFS# 06-13), Claire Giannini Fund, the Susan G. Komen Breast Cancer Foundation (SAB15-00003), Mary Kay Foundation (017-14), Skippy Frank Foundation, the Donald E. and Delia B. Baxter Foundation, Center for Cancer Nanotechnology Excellence and Translation (CCNE-T; NIH-NCI U54CA151459), Stanford Bio-X Interdisciplinary Initiative Seed Grant (IIP6-43), Chan Zuckerberg Biohub, Cancer Research supported by The Pew Charitable Trusts and The Alexander and Margaret Stewart Trust. K.Y.S. is the D. G. "Mitch" Mitchell Clinical Investigator supported by the Damon Runyon Cancer Research Foundation (CI-104-19).

Notes

The authors declare no competing financial interest.

ACKNOWLEDGMENTS

We thank Stanford Nano Shared Facilities and Stanford Nanofabrication Lab for the assistance in metasurface fabrication. We thank Dr. Aaron Hryciw for offering 'Raith_GDSII MATLAB toolbox'.

ABBREVIATIONS

OCT, optical coherence tomography; PS, polystyrene; FT, Fourier transform; ICP, inductively coupled plasma; SEM, scanning electron microscope; IPA, isopropyl alcohol; DI, deionized; RIE, reactive ion etching; fwhm, full-width-at-half-maximum; DOF, depth-of-focus; FOV, field-of-view; SNR, signal-to-noise ratio; N.A., numerical aperture.

REFERENCES

(1) Costello, F. Optical coherence tomography in neuro-ophthalmology. *Neurologic clinics* **2017**, *35* (1), 153−163.
(2) Monteiro-Henriques, I.; Rocha-Sousa, A.; Barbosa-Breda, J. Optical coherence tomography angiography changes in cardiovascular systemic diseases and risk factors: A Review. *Acta Ophthalmologica* **2022**, *100* (1), e1−e15.
(3) Spaide, R. F.; Fujimoto, J. G.; Waheed, N. K.; Sadda, S. R.; Staurenghi, G. Optical coherence tomography angiography. *Progress in retinal and eye research* **2018**, *64*, 1−55.
(4) Baran, U.; Wang, R. K. Review of optical coherence tomography based angiography in neuroscience. *Neurophotonics* **2016**, *3* (1), 010902.
(5) Tsai, T. H.; Leggett, C. L.; Trindade, A. J.; Sethi, A.; Swager, A. F.; Joshi, V.; Bergman, J. J.; Mashimo, H.; Nishioka, N. S.; Namati, E. Optical coherence tomography in gastroenterology: a review and future outlook. *Journal of biomedical optics* **2017**, *22* (12), 121716.
(6) Hsieh, Y. S.; Ho, Y. C.; Lee, S. Y.; Chuang, C. C.; Tsai, J. C.; Lin, K. F.; Sun, C. W. Dental optical coherence tomography. *Sensors* **2013**, *13* (7), 8928−8949.
(7) Wan, B.; Ganier, C.; Du-Harpur, X.; Harun, N.; Watt, F. M.; Patalay, R.; Lynch, M. D. Applications and future directions for optical coherence tomography in dermatology. *British Journal of Dermatology* **2021**, *184* (6), 1014−1022.
(8) Qi, B.; Himmer, A. P.; Gordon, L. M.; Yang, X. V.; Dickensheets, L. D.; Vitkin, I. A. Dynamic focus control in high-speed optical coherence tomography based on a microelectromechanical mirror. *Opt. Commun.* **2004**, *232* (1−6), 123−128.
(9) Liao, W.; Chen, T.; Wang, C.; Zhang, W.; Peng, Z.; Zhang, X.; Ai, S.; Fu, D.; Zhou, T.; Xue, P. Endoscopic optical coherence tomography with a focus-adjustable probe. *Opt. Lett.* **2017**, *42* (20), 4040−4043.
(10) Zhao, J.; Winetraub, Y.; Yuan, E.; Chan, W. H.; Aasi, S. Z.; Sarin, K. Y.; Zohar, O.; de la Zerda, A. Angular compounding for speckle reduction in optical coherence tomography using geometric image registration algorithm and digital focusing. *Sci. Rep.* **2020**, *10* (1), 1−11.
(11) Ralston, T. S.; Marks, D. L.; Scott Carney, P.; Boppart, S. A. Interferometric synthetic aperture microscopy. *Nat. Phys.* **2007**, *3* (2), 129−134.
(12) Curatolo, A.; Munro, P. R.; Lorenser, D.; Sreekumar, P.; Singe, C. C.; Kennedy, B. F.; Sampson, D. D. Quantifying the influence of Bessel beams on image quality in optical coherence tomography. *Sci. Rep.* **2016**, *6* (1), 1−12.
(13) Lee, K. S.; Rolland, J. P. Bessel beam spectral-domain high-resolution optical coherence tomography with micro-optic axicon providing extended focusing range. *Optics letters* **2008**, *33* (15), 1696−1698.
(14) Kim, J.; Xing, J.; Nam, H. S.; Song, J. W.; Kim, J. W.; Yoo, H. Endoscopic micro-optical coherence tomography with extended depth of focus using a binary phase spatial filter. *Opt. Lett.* **2017**, *42* (3), 379−382.
(15) Liu, L.; Gardecki, J. A.; Nadkarni, S. K.; Toussaint, J. D.; Yagi, Y.; Bouma, B. E.; Tearney, G. J. Imaging the subcellular structure of human coronary atherosclerosis using micro−optical coherence tomography. *Nature medicine* **2011**, *17* (8), 1010−1014.
(16) Standish, B. A.; Lee, K. K.; Mariampillai, A.; Munce, N. R.; Leung, M. K.; Yang, V. X.; Vitkin, I. A. In vivo endoscopic multi-beam optical coherence tomography. *Physics in Medicine & Biology* **2010**, *55* (3), 615.
(17) Zhao, J.; Winetraub, Y.; Du, L.; Van Vleck, A.; Ichimura, K.; Huang, C.; Aasi, S. Z.; Sarin, K. Y.; de la Zerda, A. Flexible method for generating needle-shaped beams and its application in optical coherence tomography. *Optica* **2022**, *9* (8), 859−867.
(18) Cao, R.; Zhao, J.; Li, L.; Du, L.; Zhang, Y.; Luo, Y.; Jiang, L.; Davis, S.; Zhou, Q.; de la Zerda, A.; Wang, L. V. Optical-resolution photoacoustic microscopy with a needle-shaped beam. *Nat. Photonics* **2023**, *17*, 89.
(19) Tognetti, L.; Cinotti, E.; Falcinelli, F.; Miracco, C.; Suppa, M.; Perrot, J. L.; Rubegni, P. Line-field confocal optical coherence tomography: a new tool for non-invasive differential diagnosis of pustular skin disorders. *Journal of the European Academy of Dermatology and Venereology* **2022**, *36* (10), 1873−1883.
(20) Badon, A.; Bensussen, S.; Gritton, H. J.; Awal, M. R.; Gabel, C. V.; Han, X.; Mertz, J. Video-rate large-scale imaging with Multi-Z confocal microscopy. *Optica* **2019**, *6* (4), 389−395.
(21) Yang, W.; Miller, J. E. K.; Carrillo-Reid, L.; Pnevmatikakis, E.; Paninski, L.; Yuste, R.; Peterka, D. S. Simultaneous multi-plane imaging of neural circuits. *Neuron* **2016**, *89* (2), 269−284.
(22) Li, Y.; Wong, T. T.; Shi, J.; Hsu, H. C.; Wang, L. V. Multifocal photoacoustic microscopy using a single-element ultrasonic transducer through an ergodic relay. *Light: Science & Applications* **2020**, *9* (1), 1−7.
(23) Engelberg, J.; Levy, U. The advantages of metalenses over diffractive lenses. *Nat. Commun.* **2020**, *11* (1), 1−4.
(24) Park, J. S.; Zhang, S.; She, A.; Chen, W. T.; Lin, P.; Yousef, K. M.; Cheng, J. X.; Capasso, F. All-glass, large metalens at visible wavelength using deep-ultraviolet projection lithography. *Nano Lett.* **2019**, *19* (12), 8673−8682.
(25) Chen, S.; Liu, W.; Li, Z.; Cheng, H.; Tian, J. Metasurface-empowered optical multiplexing and multifunction. *Adv. Mater.* **2020**, *32* (3), 1805912.
(26) Zhang, S.; Wong, C. L.; Zeng, S.; Bi, R.; Tai, K.; Dholakia, K.; Olivo, M. Metasurfaces for biomedical applications: imaging and

https://doi.org/10.1021/acsnano.2c09542
ACS Nano 2023, 17, 3442−3451

sensing from a nanophotonics perspective. *Nanophotonics* **2020**, *10* (1), 259−293.
(27) Moon, S. W.; Kim, Y.; Yoon, G.; Rho, J. Recent progress on ultrathin metalenses for flat optics. *Iscience* **2020**, *23* (12), 101877.
(28) Lee, D.; Gwak, J.; Badloe, T.; Palomba, S.; Rho, J. Metasurfaces-based imaging and applications: from miniaturized optical components to functional imaging platforms. *Nanoscale Advances* **2020**, *2* (2), 605−625.
(29) Zhang, S.; Wong, C. L.; Zeng, S.; Bi, R.; Tai, K.; Dholakia, K.; Olivo, M. Metasurfaces for biomedical applications: imaging and sensing from a nanophotonics perspective. *Nanophotonics* **2020**, *10* (1), 259−293.
(30) Zhou, Y.; Zheng, H.; Kravchenko, I. I.; Valentine, J. Flat optics for image differentiation. *Nat. Photonics* **2020**, *14* (5), 316−323.
(31) Pahlevaninezhad, H.; Khorasaninejad, M.; Huang, Y. W.; Shi, Z.; Hariri, L. P.; Adams, D. C.; Ding, V.; Zhu, A.; Qiu, C. W.; Capasso, F.; Suter, M. J. Nano-optic endoscope for high-resolution optical coherence tomography in vivo. *Nat. Photonics* **2018**, *12* (9), 540−547.
(32) Bezryadina, A.; Zhao, J.; Xia, Y.; Zhang, X.; Liu, Z. High spatiotemporal resolution imaging with localized plasmonic structured illumination microscopy. *ACS Nano* **2018**, *12* (8), 8248−8254.
(33) Arbabi, E.; Li, J.; Hutchins, R. J.; Kamali, S. M.; Arbabi, A.; Horie, Y.; Van Dorpe, P.; Gradinaru, V.; Wagenaar, D. A.; Faraon, A. Two-photon microscopy with a double-wavelength metasurface objective lens. *Nano Lett.* **2018**, *18* (8), 4943−4948.
(34) Pahlevaninezhad, M.; Huang, Y. W.; Pahlevani, M.; Bouma, B.; Suter, M. J.; Capasso, F.; Pahlevaninezhad, H. Metasurface-based bijective illumination collection imaging provides high-resolution tomography in three dimensions. *Nat. Photonics* **2022**, *16* (3), 203−211.
(35) Tan, S.; Yang, F.; Boominathan, V.; Veeraraghavan, A.; Naik, G. V. 3D imaging using extreme dispersion in optical metasurfaces. *ACS Photonics* **2021**, *8* (5), 1421−1429.
(36) Zou, X.; Zheng, G.; Yuan, Q.; Zang, W.; Chen, R.; Li, T.; Li, L.; Wang, S.; Wang, Z.; Zhu, S. Imaging based on metalenses. *PhotoniX* **2020**, *1* (1), 1−24.
(37) Presutti, F.; Monticone, F. Focusing on bandwidth: achromatic metalens limits. *Optica* **2020**, *7* (6), 624−631.
(38) Siraji, A. A.; Zhao, Y., 2022. Scalar Diffraction Analysis of Dispersion In Low-Index Thin Flat Lenses. *arXiv (Optics)*, 2204.11398, ver. 1. https://arxiv.org/abs/2204.11398 (accessed 04/25/2022).
(39) Chen, W. T.; Zhu, A. Y.; Sisler, J.; Huang, Y. W.; Yousef, K. M.; Lee, E.; Qiu, C. W.; Capasso, F. Broadband achromatic metasurface-refractive optics. *Nano Lett.* **2018**, *18* (12), 7801−7808.
(40) Sawant, R.; Andrén, D.; Martins, R. J.; Khadir, S.; Verre, R.; Käll, M.; Genevet, P. Aberration-corrected large-scale hybrid metalenses. *Optica* **2021**, *8* (11), 1405−1411.
(41) Castro, R. P.; Stephens, A.; Fraga-Braghiroli, N. A.; Oliviero, M. C.; Rezze, G. G.; Rabinovitz, H.; Scope, A. Accuracy of in vivo confocal microscopy for diagnosis of basal cell carcinoma: a comparative study between handheld and wide-probe confocal imaging. *Journal of the European Academy of Dermatology and Venereology* **2015**, *29* (6), 1164−1169.
(42) González, S.; Tannous, Z. Real-time, in vivo confocal reflectance microscopy of basal cell carcinoma. *Journal of the American Academy of Dermatology* **2002**, *47* (6), 869−874.
(43) Peppelman, M.; Wolberink, E. A.; Blokx, W. A.; Van De Kerkhof, P. C.; Van Erp, P. E.; Gerritsen, M. J. P. In vivo diagnosis of basal cell carcinoma subtype by reflectance confocal microscopy. *Dermatology* **2013**, *227* (3), 255−262.
(44) Khorasaninejad, M.; Shi, Z.; Zhu, A. Y.; Chen, W. T.; Sanjeev, V.; Zaidi, A.; Capasso, F. Achromatic metalens over 60 nm bandwidth in the visible and metalens with reverse chromatic dispersion. *Nano Lett.* **2017**, *17* (3), 1819−1824.
(45) Wang, S.; Wu, P. C.; Su, V. C.; Lai, Y. C.; Chen, M. K.; Kuo, H. Y.; Chen, B. H.; Chen, Y. H.; Huang, T. T.; Wang, J. H.; Lin, R. M.; et al. A broadband achromatic metalens in the visible. *Nature Nanotechnol.* **2018**, *13* (3), 227−232.
(46) Chen, W. T.; Zhu, A. Y.; Capasso, F. Flat optics with dispersion-engineered metasurfaces. *Nature Reviews Materials* **2020**, *5* (8), 604−620.
(47) Jonnal, R. S.; Kocaoglu, O. P.; Zawadzki, R. J.; Liu, Z.; Miller, D. T.; Werner, J. S. A review of adaptive optics optical coherence tomography: technical advances, scientific applications, and the future. *Investigative ophthalmology & visual science* **2016**, *57* (9), OCT51−OCT68.
(48) Liu, W.; Ma, D.; Li, Z.; Cheng, H.; Choi, D. Y.; Tian, J.; Chen, S. Aberration-corrected three-dimensional positioning with a single-shot metalens array. *Optica* **2020**, *7* (12), 1706−1713.
(49) Chen, S.; Li, Z.; Liu, W.; Cheng, H.; Tian, J. From single-dimensional to multidimensional manipulation of optical waves with metasurfaces. *Adv. Mater.* **2019**, *31* (16), 1802458.
(50) Liu, W.; Li, Z.; Li, Z.; Cheng, H.; Tang, C.; Li, J.; Chen, S.; Tian, J. Energy-tailorable spin-selective multifunctional metasurfaces with full Fourier components. *Adv. Mater.* **2019**, *31* (32), 1901729.

https://doi.org/10.1021/acsnano.2c09542
ACS Nano 2023, 17, 3442−3451